Attitude Determination for Small Satellites with Modest Pointing Constraints

Todd E. Humphreys, Utah State University
Advisors: Dr. Rees Fullmer and Dr. Charles Swenson

Abstract— **This monograph reports on the development of the attitude determination backbone of the Ionospheric Observation Nanosatellite Formation (ION-F). Three spacecraft with similarly modest pointing constraints comprise the ION-F constellation. Pointing requirements for the constellation are dictated by the formation flying mission objective and communication demands. To satisfy pointing requirements the attitude control system for each spacecraft will require attitude estimates with accuracies on the order of 1 degree. An investigation into sensor suites capable of satisfying this requirement within the additional monetary, mass, and power constraints imposed by the ION-F program was carried out. Ultimately, a gyroless magnetometer-based Kalman filter was chosen as the attitude determination backbone. A high fidelity simulation created specifically for ION-F spacecraft revealed the filter was capable of attitude errors below 1.6° (1σ) and rate errors below $0.006\ \frac{deg}{sec}$. Further tests using actual telemetered data from the Danish Ørsted satellite were performed with satisfactory results. Other sensors may be added to this backbone to increase accuracy and speed filter convergence. For example, the possibility of incorporating solar panel data into the filter was examined. It was concluded that under fairly general conditions solar panel data speeds initial filter convergence and may also be used to estimate magnetometer mounting misalignments. Although designed for the ION-F constellation, the attitude determination system described in this paper is generically applicable to many small spacecraft in inclined low-earth orbit. The 1-2 degree accuracy of which the system is capable lends itself well to small satellite applications such as formation flying and imaging or docking with other spacecraft.**

I. Introduction

SMALL spacecraft (SC) entered a new era with the initiation of the AFSOR/DARPA University Nanosatellite Program (UNP) . Several universities were awarded the challenge of designing SC of the nanosatellite weight class (approximately 10 kg) under tight budget constraints using primarily student labor. This much has been done before. Stanford and the University of Alabama, among others, have already launched student-built SC with encouraging results. But never before have university SC been as ambitious in their design and declared mission objectives as those involved in the UNP. The SC comprising the ION-F constellation (under the auspices of the UNP) are a good example of this ambition. The University of Washington/Cornell's DAWGSTAR, Virginia Polytechnic Institute's HOKIESAT, and Utah State University's USUSAT are each SC of extraordinary power and complexity. If successful, the ION-F SC will be the first student-built 3-axis stabilized SC. Within industry, ION-F is preceded in 3-axis stabilization only by Surrey Satellite Technology's SNAP for the nanosatellite weight class. Other nanosatellite platforms have invariably depended on passive gravity gradient or spin stabilization.

The AD system for the ION-F cluster has been designed to exploit the capability of the ION-F SC, while satisfying several constraints imposed by the UNP. In the sequel, the design of the backbone AD system for ION-F is detailed. The design is tested by simulation and results are presented, along with results of tests using actual satellite data. Possible hardware additions to the AD backbone are considered. The use of body-mounted solar cells is given particular attention owing to their ubiquity on small SC. An appendix is also provided wherein the more tedious details of the magnetometer-based Kalman filter are found.

II. Sensor Suite Selection

External constraints imposed on the ION-F AD system may be divided into three categories: Price, Poundage, and Power. The tight budget under which the ION-F SC were designed and built militated against the use of costly AD hardware. As a result, the sensor suites of the SC are comprised of non-redundant less accurate components with little or no flight heritage. Mass constraints, limiting each of the SC to an approximate 15 kg, also discouraged the use of larger, more accurate, or redundant sensors. Finally, the small surface area of the ION-F SC translated into a tight power budget. This is most severe for the smaller USUSAT, whose nominal available power will be 12 Watts.

Initially, a triad of quartz vibratory rate gyroscopes was considered an essential component of the AD backbone. These gyros would enable rapid kinetic energy dumping during detumble and provide a consistent rate input to the AD routines throughout the rest of the mission. However, consideration of the gyros cost, mass, and power requirements demanded a compelling reason to include them on the SC [1]. This was especially true for USUSAT, where the power demands of the most practical Systron Donner QRS11 gyros represented 20% of the overall power budget. These compelling reasons were never found. A clever approach to detumble relying solely on magnetometer measurements (the so-called B-dot algorithm) has been shown to adequately dissipate initial SC kinetic energy, while proper filtering techniques based on magnetometer measurements provide a continuously available rate estimate accurate to within $0.006\frac{deg}{sec}$.

The accuracy of vibratory microgyroscopes suitable for small SC has not yet been reached to the point where these should be considered an essential member of the AD sensor suite. Most notable are large turn-on rate biases and significant bias instability (0.5 to 2 $\frac{deg}{sec}$ and 7 $\frac{deg}{hr}$ respec-

tively for the QRS11). Several institutions such as NASA's Jet Propulsion Laboratory and British Aerospace are proceeding with development of accurate low-cost vibratory microgyros, but the trend has been that size and power reductions equal signal-to-noise ratio reductions which degrade accuracy. Within a decade, these challenges will most likely be surmounted and inclusion of gyros on small SC will become the *status in quo*.

The three-axis magnetometer (TAM) is an indispensable element in any AD sensor suite. Almost every attitude-controlled SC since NASA's 1979 MAGSAT mission has included some type of magnetic field sensor. The TAM provides a continuously available two-axis attitude measurement with surprising accuracy (details of expected TAM accuracy will be discussed in a later section). The TAM's relative low cost and almost insignificant power demand (300 mA for the Applied Physics model 533 [2]) further increase its appeal. For these reasons, the AD backbone discussed in this work is based on TAM measurements.

Other useful AD sensors suitable for small SC include sun, horizon, star, and differential GPS sensors. The latter constitutes another continuously available attitude source, but may not yet be suitable for small SC owing to the need to resolve phase ambiguities and the large number of required GPS channels [3]. Sun and horizon sensors in the form of small CMOS cameras have been developed for use on the ION-F SC. While not considered part of the ION-F AD backbone because of their intermittency, algorithmic complexity, and lack of flight heritage, the sun and horizon cameras offer the exciting prospect of sub-degree accuracy and will be included in the ION-F AD estimate if they prove themselves during SC commissioning.

The CMOS star camera [4] is the ultimate desideratum of a small SC AD platform. Several of these cameras mounted strategically would afford nearly continuous 3-axis SC attitude knowledge. Prototype development continues along these lines, with star measurements in the face of angular rates posing the most daunting challenge. The CMOS star camera acts as an integrator of photons impingent on its collector array. Background thermal noise requires either long integration times or cooling/focusing equipment in order to detect a sufficient number of stars to provide reliable sensing. When the SC is rotating, long integration times translate into streaks instead of points on the collector array. Presently, this would limit SC rotation rates to under $0.1\frac{deg}{sec}$. Clearly, the CMOS star camera will not constitute a *panacea* for small SC AD, but will augment an AD backbone capable of continuously available rate estimates.

III. Filter Design

A. Description

With the TAM as primary sensor for the ION-F AD backbone, it was necessary to design a magnetometer-based extended Kalman filter (MEKF) capable of accurate attitude estimates. One such approach was introduced in the seminal work by Psiaki et al. [5] where a Kalman filtering scheme for three-axis estimation based solely on TAM data is developed. Although only two axes of attitude information are simultaneously measurable using a TAM, Psiaki demonstrates that for moderately inclined orbits the SC attitude, rate, and constant disturbance torques are (weakly) observable through proper filtering of the TAM data. Application of this filter is limited to nadir-pointing gravity-gradient stabilized SC, however, since linearization of the SC dynamics and measurement sensitivity functions, in addition to the weak state observability, leads to instability for wide initial mispointing angles. With the gravity gradient boom, the SC is able to right itself to within a capture envelope of the assumed initial orientation. Psiaki demonstrates good convergence for mispointings below 45° and possible convergence up to 60°.

The filter reported in this monograph is similar to the one originally introduced by Psiaki, but includes several modifications which allow more universal convergence. The structure of the filter is modified to handle mispointings beyond 90° and innovations not conforming to the small-angle assumption of the EKF. Filter updates are slightly modified to decrease the probability of covariance matrix explosion, while a failsafe reset allows for this contingency.

Due to the tedium involved in setting up and deriving the extended Kalman filter applied to TAM measurements, details of the filter are included in the appendix. In brief, the full filter state is composed of 10 elements: The four quaternion elements, a rate vector estimate, and a disturbance torque estimate:

$$x = \begin{bmatrix} \bar{q} \\ \omega \\ n_d \end{bmatrix} \tag{1}$$

The quaternion and rate vector are necessary for attitude control, while the disturbance torque estimate adds robustness to the filter by estimating the magnitude and direction of slowly varying disturbance torques. A reduced state excluding one of the redundant quaternion elements is used in the linearized Kalman filter. Measurement innovations for the linearized filter are based on the arithmetic difference between expected and actual magnetic field readings (not the cross-product as in [5]), allowing initial mispointings up to 180°.

B. Implementation

Filter implementation follows the pattern outlined in section VIII-D of the appendix with slight modification. The state vector estimate $\hat{x}_{k|k}$ is propagated as usual with numerical integration to yield $\hat{x}_{k+1|k}$. However, when the body-referenced state error estimate, $\Delta\hat{\tilde{x}}_{k+1|k+1}$ is to be combined with $\hat{x}_{k+1|k}$ to yield an updated state estimate, care must be taken to combine the quaternions properly. The rate and disturbance torque components of the estimate are added as usual:

$$\hat{\omega}_{k+1|k+1} = \hat{\omega}_{k+1|k} + \Delta\hat{\omega}_{k+1|k+1} \tag{2}$$

$$\hat{n}_{d\ k+1|k+1} = \hat{n}_{d\ k+1|k} + \Delta\hat{n}_{d\ k+1|k+1} \tag{3}$$

but the updated quaternion is formed by

$$\hat{\bar{q}}_{k+1|k+1} = \begin{bmatrix} \delta\hat{q}_{k+1|k+1} \\ \sqrt{1-||\delta\hat{q}_{k+1|k+1}||^2} \end{bmatrix} \otimes \hat{\bar{q}}_{k+1|k} \tag{4}$$

During initial convergence, the argument of the square root in (4) may become negative, meaning the small angle assumption has been violated by a large mispointing. When this condition is detected, the estimated error quaternion is written instead as

$$\frac{1}{\sqrt{1+||\delta\hat{q}_{k+1|k+1}||^2}} \begin{bmatrix} \delta\hat{q}_{k+1|k+1} \\ 1 \end{bmatrix} \tag{5}$$

The more accurate update (4) is again adopted as the filter settles and $||\delta\hat{q}_{k+1|k+1}||^2$ decreases below unity.

Also during initial convergence, the error covariance matrix P may become very large due to violations of the small angle approximation. This is mitigated by starting the algorithm with an initial *measurement update* before performing the first *time update*. Also, the re-calculation of the H_k matrix using the filtered state estimate as mentioned in section VIII-D helps reduce the size of P at each sample step. Simulation has demonstrated that for some initial conditions, however, these countermeasures are not failsafe, and it becomes necessary to reset P and $\hat{x}$ to their initial values, i.e., $P_{k+1|k+1} = P_{0|0}$, $\hat{x}_{k+1|k+1} = \hat{x}_{0|0}$. This reset is effected when the trace of P exceeds a predetermined threshold.

IV. Simulation

A high fidelity simulation was chosen as means to test the MEKF. Linear analysis of the MEKF is limited in its ability to predict filter accuracy and stability for the varying biases, initial conditions, and disturbances encountered in practice. For a thorough linear analysis, the reader is referred to [5].

A. Simulation Structure and Error Modeling

Simulations were carried out in Matlab *Simulink* using a simulator designed specifically for the ION-F SC. An outline of the simulator structure is seen in Fig. 1. The *Satellite Dynamics and Time* block generates SC attitudes and ephemerides using a three degree-of-freedom satellite rotational model and a two-body orbit propagator, while providing time elapsed since January 1, 2000 and since the epoch of simulation. The *Estimation Algorithms* block contains Kalman filtering routines. The *Attitude Sensors* block is a motley collection of sensor simulators and inertial vector calculators. Solar ephemerides are calculated within this block using the algorithm presented in [6] to a precision of 0.01°. Inertial magnetic field vectors are simulated using a 10th-order IGRF model. TAM, solar panel, sun camera, and horizon camera readings are simulated using appropriate additive noise and biases. Albedo impingent on the solar panels is calculated assuming a diffusely radiating sphere [7] and a time varying albedo factor [8]. Shadowing effects are also taken into account for USUSAT's particular dual-boom structure.

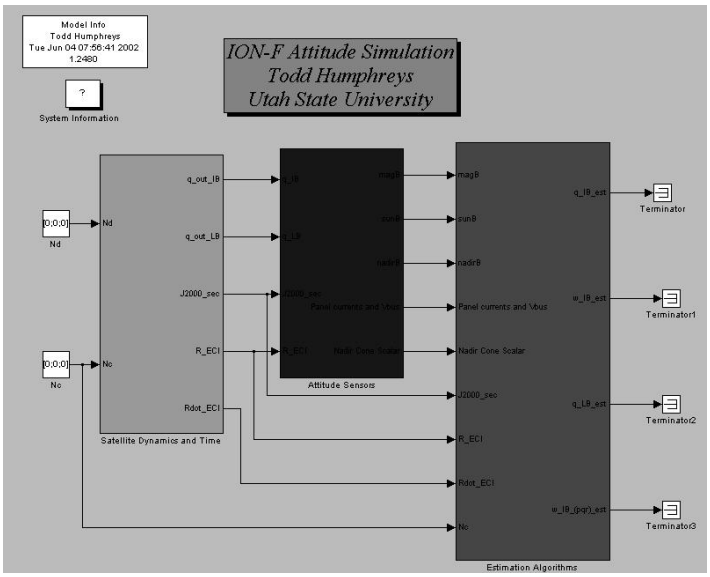

Fig. 1. Simulation testbed for ION-F spacecraft.

Probable magnetic measurement related errors were calculated as shown in table I. Entries marked *calibrated* assume an onboard calibration routine presented in section VI has reduced biases, scale factors, and nonorthogonalities to the displayed levels.

TABLE I
Magnetic Field Estimation and Measurment Error Sources.

Source	**RMS Value(deg)**
Modeling error (10th order)	0.1
In-track orbit uncertainty	0.384
Onboard magnets	0.5 (calibrated)
TAM noise	0.0077
12-bit quantization	0.027
Scale Factor	negligible (calibrated)
Orthogonality and alignment	0.5 (calibrated)
RSS Total	0.81

It would be ingenuous to simulate the above errors by simply adding an uncorrelated error source producing an equivalent total RMS value of 0.81° to the simulation. Many of the above error sources are highly time-correlated. The Kalman filter deals much less effectively with time-correlated noise than with white noise sources. To approximate the autocorrelation of the above sources, two IGRF field models were used. The truth model was chosen as a 10th order IGRF model. The estimated field was a 6th order IGRF model with coefficients offset from the truth epoch by 5 years. This results in time-correlated magnetic field errors with an RMS value close to 0.81°, as seen in Fig. 2.

The filter was applied successfully to several different SC models, but most extensively tested using the speci-

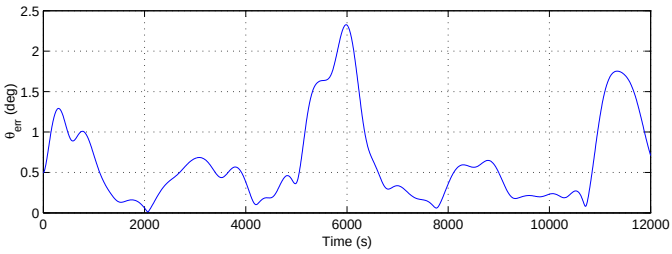

Fig. 2. Typical magnetic field model error (deg) using a 10th order truth model and 6th order, 5 year offset estimation model.

fications for USUSAT (15 kg, 51°, 400 km circular orbit, $I_{xx} = I_{yy} = 0.85$, $I_{zz} = 1.6$ kg-m^2).

B. Filter Tuning

The parameters $P_{0|0}$, R, and Q within the EKF may be modified to optimize its performance for a given application. These parameters must be chosen judiciously to balance inherent tradeoffs involved. For a linear Kalman filter, $P_{0|0}$ may be chosen arbitrarily large, with the rate of convergence increasing with larger $P_{0|0}$. When nonlinear dynamics and measurement equations are linearized in the EKF, however, it is implicitly assumed that the initial state estimate is close to the actual initial state, and a large $P_{0|0}$ causes the filter to diverge. Steady-state performance of the EKF is most directly linked to the process noise covariance matrix Q, which reflects disturbances and possible uncertainty in the SC dynamics model. In the face of white Gaussian process and measurement noise, one would increase the value of the diagonal elements of Q to add robustness and increase the bandwidth of the filter, and decrease Q to improve accuracy. When noise sources are non-Gaussian and non-white, changing the values in Q has a less predictable effect. For the present filter, tuning proceeded as follows: The diagonal elements of $P_{0|0}$ were chosen slightly less than the square of the expected errors in the initial state vector $\hat{x}_{0|0}$. All off-diagonal elements are set to zero. The diagonal elements of R are chosen to reflect measurement error. For the magnetic field vector, these values are obtained by comparing the magnetic field truth model against the estimation model. For other sensor measurements corresponding diagonal elements of R reflect expected error contributions. Off-diagonal elements are set to zero. The elements of Q corresponding to the vector part of the error quaternion are set to zero. The remaining six diagonal elements are initialized with the square of expected rate and torque errors, and then tuned to balance robustness and accuracy objectives.

C. Filter Evaluation

Extensive Monte-Carlo simulation was performed on the filter. Initial attitude and rates were varied, as well as simulation epoch and RAAN. Initial rates were bounded between 0.03 and 3 $\frac{deg}{sec}$. No knowledge of initial attitude or rates was assumed.

Using TAM data alone, the filter invariably converged to less than 5°, usually in less than one orbit. A typical example of this is given in Fig. 3.

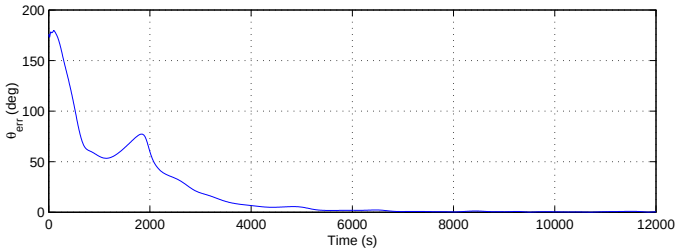

Fig. 3. Typical convergence of magnetometer-only EKF.

A zoomed view of the latter half of Fig. 3 is provided in Fig. 4 to demonstrate steady-state accuracy. The filter performs within a 1.6° (1σ) envelope. The filter's evaluation of angular rates was especially good. Steady-state accuracies less than 0.006 $\frac{deg}{sec}$ were typical.

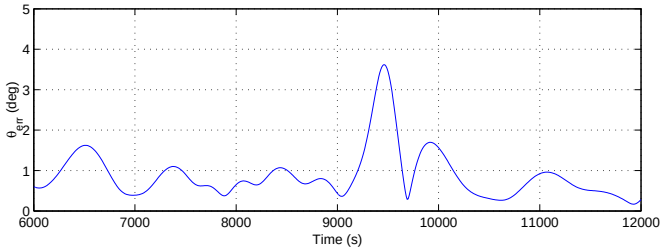

Fig. 4. A zoomed view of the second orbit of Fig. 12 (deg).

Filter robustness was evaluated by subjecting the dynamic model of the SC to a slowly varying external disturbance torque. Given the geometry and altitude of USUSAT, the only non-negligible disturbance torque will be aerodynamic. Assuming a 2 cm offset between the center of pressure of the largest panel and the SC center of mass, a 1 μ N-m disturbance torque is reasonable. A sinusoidally varying disturbance torque with such an amplitude was applied to the body X-axis. The results of this are displayed in Figs. 5 and 6. They demonstrate good estimation of the input torque, and little effect on overall accuracy.

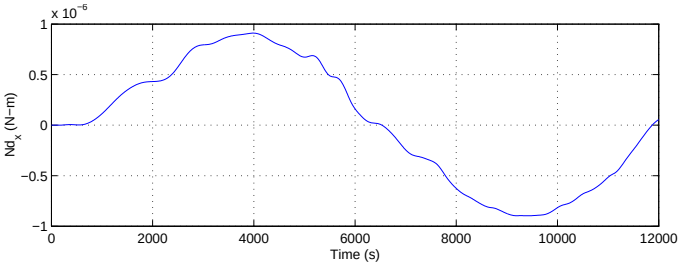

Fig. 5. The magnetometer-only filter is able to accurately estimate a 1 μN-m amplitude slowly varying sinusoidal input torque on the body X- axis.

Robustness of the filter was also demonstrated by adding uncertainty to the SC inertia tensor. A 10% moment of inertia variation on each axis produced negligible

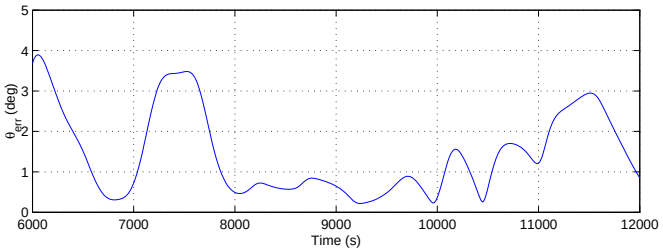

Fig. 6. Steady state error for case with varying $1\,\mu$N-m disturbance torque shows satisfactory filter performance in the face of external disturbances. (deg)

changes in steady-state accuracy. This is due to the filter's ability to model inertia mismatching as a disturbance torque.

Filter performance was also evaluated using actual TAM data from the Danish Ørsted satellite, launched in February of 1999 (62 kg, 96.6°, 600-850 km elliptical orbit, $I_{xx} = 2192, I_{yy} = 2196$, $I_{zz} = 1.5$ kg-m^2). Ørsted enjoys a 6 m boom for gravity gradient stabilization and TAM isolation. A high precision compact spherical coil magnetometer is mounted at the end of the boom. Despite the highly accurate magnetic field readings, determination of the Ørsted attitude represented a challenge to the MEKF because no knowledge of attitude control torques was available to the filter. The filter is well suited to estimate slowly varying (such as sinusoids at the orbital period) disturbance torques, but cannot estimate rapidly changing disturbances unless a tradeoff is made that degrades steady-state filter accuracy. Inspection of the Ørsted attitude profile reveals that on several occasions during the data span used in simulation the magnetic torquing rods were activated to trim SC orientation. Moreover, the inertia tensor used to model Ørsted dynamics was only approximate, and no attempt was made to re-tune the filter noise parameters–these were left as for USUSAT. The truth model for the Ørsted data was taken from attitude estimates produced by a star imager mounted close to the TAM. The results of the simulation are shown in Fig. 7. Evidently, the filter converges rapidly and performs within a 10° steady-state error envelope. This is satisfactory given the incomplete knowledge of control torques mentioned above.

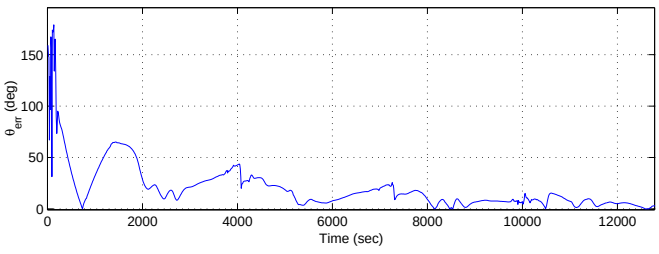

Fig. 7. Filter evaluation using actual magnetometer data from Ørsted. The filter converges rapidly and is sufficiently accurate given incomplete knowledge of control torques.

V. Filter Convergence Issues

The results of the evaluation of the MEKF presented above are somewhat specious. It is mentioned that the EKF "usually" converges in less than one orbit. This would naturally lead one to inquire into "unusual" convergence. With the weak state observability provided by TAM and the highly nonlinear relationship between the measured magnetic field vector and SC attitude, pathological cases arise wherein convergence does not take place within one orbit. These cases are made more infrequent by the several enhancements to the filter mentioned in section III-A (and more thoroughly in the appendix), but cannot be wholly avoided unless filter robustness against disturbance torques is to be sacrificed. This is one of the tradeoffs inherent in filter tuning. These types of pathological cases arose with a frequency of about 1:15 during simulation. One such case may be seen in Fig. 8. The filter eventually converged in just over two orbits (13,000 sec), but this type of belated convergence is, well, unsettling.

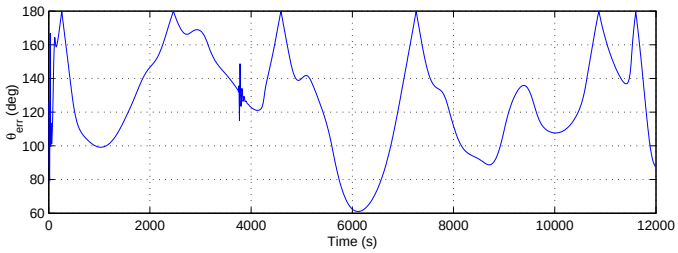

Fig. 8. Delayed convergence case using magnetometer data only. The filter eventually settled just after two orbits (13,000 sec)

There exist several methods to deal with the erratic convergence of MEKFs. Surrey Satellite Technology's SNAP nanosatellite was equipped with a MEKF [10]. The approached used by the SNAP team lead by W.H. Steyn was to place the the SC in a Y-Thompson (fixed nadir pointing) state. A specially designed pitch filter was then employed to estimate the pitch angle. A full state EKF was then initialized with the known SC attitude. This method worked well in practice onboard the SNAP SC. It is not meant to converge in less than one orbit, however.

Another alternative is introduced by M. Challa et al. in [11]. In this approach, the MEKF is primed using the well-known deterministic TRIAD algorithm. The TRIAD algorithm is a single-frame attitude estimator requiring two reference vectors as input. Although only the magnetic field vector is instantaneously available, Challa and his colleagues were able to cleverly extract a pseudo-vector from the derivative of the magnetic field vector using batch measurements. This method has yet to be tested in flight and introduces some computational complexity, but provides very rapid convergence (less than 500 seconds) and has proven itself when applied to telemetry from orbiting SC.

For the ION-F SC, another method was employed that makes use of already available attitude hardware–the

body-mounted solar panels. This approach was taken to investigate the utility of solar panels as sun sensors. If sufficiently accurate, the solar panels might also be used to counter another shortcoming of the MEKF–possible TAM reference frame misalignments (these will be discussed shortly).

A. Solar Panels as Attitude Sensors

It is well known that the ratio of measured solar panel current to the current at normal sunlight incidence is approximately equal to the cosine of the angle of the incident sunlight. i.e.,

$$\cos(\theta) \approx \frac{I_{sc}(\theta)}{I_{sc}(0)} \tag{6}$$

Here, $I_{sc}(\theta)$ is the short-circuit current of a set of solar cells forming a panel with incident sunlight arriving at an angle θ from normal. Once this ratio is obtained, a scalar measurement is passed to the EKF as described in section VIII-E, immediately increasing state observability. Short-circuit current is not directly observable from the solar panels as these are connected to the SC bus and are under constant load. If certain parameters of the solar cells are known, however, it is possible to extract I_{sc} from the relation

$$I_{sc}(\theta) = I_L(\theta) + I_o(e^{kV_L(\theta)} - 1) \tag{7}$$

which is the standard diode equation model adapted for solar cells. The current off each panel under load and the bus voltage (I_L and V_L) are measured onboard the SC and combined with the parameters k and I_o which are determined for each panel before launch. These may be computed empirically if a sun-simulating lamp is available ($30,000.00 price tag). They may also be computed using the manufacturer's specifications at normal sunlight incidence for maximum-power voltage and current ($V_{mp}(0)$ and $I_{mp}(0)$), short-circuit current ($I_{sc}(0)$) and open-circuit voltage $V_{oc}(0)$ for each cell.

The accuracy of angular measurements from the solar cells is directly related to the precision with which $I_{sc}(0)$, k, and I_o are known. Accuracy is also related to the sensitivity of the arc-cosine function, which increases as sunlight approaches normal. To set ideas, consider a 1.2% error in estimating $I_{sc}(0)$. Manufacturer's specs for each solar cell could give rise to such an error because solar cells are often categorized in groups spanning several milliamps [9]. Angular error bounds resulting from a 1.2% error in $I_{sc}(0)$ are plotted in Fig. 9. The significance of sensitivity near normal incidence is apparent.

Accuracy is further complicated by the slight non-cosineness of the current rolloff with increasing incidence angles. To investigate this effect further, a machinists table was used to position a mockup satellite to precisely known orientations with respect to the sun and an incidence angle test was conducted. The setup for the experiment is shown in Fig. 10 with the cosine rolloff for each cell shown in Fig. 11. A second-order polynomial was found to fit this data well, which allowed the quadratic

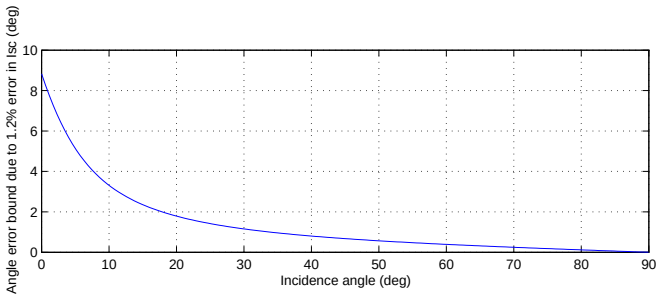

Fig. 9. Angle error bounds due to a 1.2% error in estimating $I_{sc}(0)$

formula to be used instead of the arc-cosine function to extract angles from current ratios. After the incidence angle test, the SC was positioned in several arbitrary orientations with respect to the sun. A conical intersection algorithm was applied to the current ratios from the solar cells taken two at a time, and the sun vector was routinely pinpointed to within 5°.

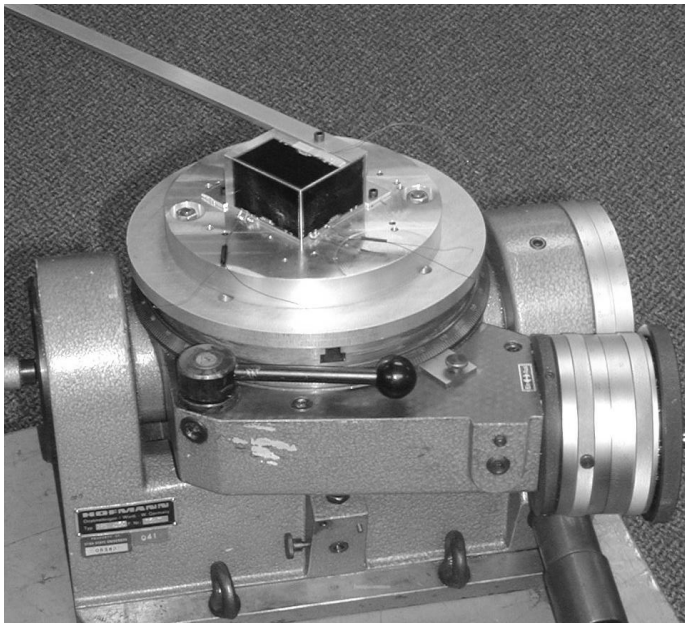

Fig. 10. Setup for sun vector tests using solar panels. Visible are the mock satellite, machinists table, and pointing boom.

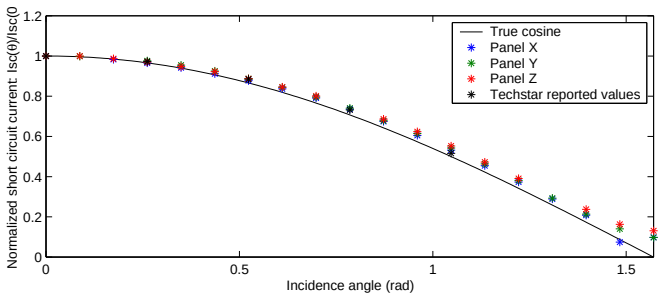

Fig. 11. Rolloff of current ratio with incidence angle is slightly above cosine.

Possibly the most egregious of all error contributors to solar panel-extracted scalar measurements is earth albedo.

Both albedo and shadowing effects were included as part of the simulation applied to the ION-F SC. Taking all of these error sources in aggregate, one may conclude that solar panel data is roughly an order of magnitude less accurate than TAM data. It was found that continuous use of solar panel measurements in the EKF only corrupted the steady-state estimate. This is due to the strong time correlation of albedo-induced noise, which makes averaging difficult. It was found most useful to incorporate solar panel data in the EKF only as needed. Necessity is established by observing at each time step the elements of the innovation vector Δz_k corresponding to the scalar solar panel measurements. If these innovations exceed expected albedo contributions by a predetermined threshold, a flag is set. While the flag is set, solar panel data is incorporated into the EKF. The flag remains set until the sun is no longer available, or the innovations become sufficiently small over a sufficiently long span, at which time the flag is cleared and the filter uses TAM data only. Incorporation of the solar panel data serves a dual purpose: Initial convergence time is decreased and attitude anomalies arising in steady-state may be detected more easily using this second independent reference.

It should be noted that within the construct of the EKF even one sunlit solar panel can provide useful data. At least two sunlit solar panels are required, in addition to the TAM data, to uniquely determine the SC attitude, but one panel often reduces the estimate error significantly, allowing the MEKF to converge.

Augmented by solar panel data, the MEKF was applied to the pathological case of Fig. 8. The result is displayed in Fig. 12, along with a plot of sun availability and intensity for each panel. With the increased observability, the filter converges very rapidly. Extensive simulations of this sort were carried out, and for each case tested, the filter converged to less than 5° within one orbit.

It should be noted that the backbone MEKF structure lends itself readily to additional vector or scalar measurements (besides the solar panels). For example, sun and horizon sensor measurements, as well as star camera data are easily folded into the MEKF backbone.

VI. Magnetometer Calibration

One final hurdle to using the MEKF for attitude estimates with accuracies of approximately 1° has to do with TAM calibration. This is accomplished in two parts. First, TAM biases, scale factors, and internal nonorthogonalities are estimated using a Kalman filter that functions independent of SC orientation [12]. The measured and expected magnetic field magnitude are differenced and this scalar value constitutes the innovation for the Kalman filter.

A second calibrating Kalman filter is used to estimate TAM reference frame misalignments. The reference marks on the outside of inexpensive TAMs may be up to 2° offset from the internal TAM reference frame [2]. This condition may be further exacerbated by mounting errors. Unless one has access to precision magnetic field simulation facilities, these misalignments must be calibrated on orbit. In contrast to the first calibration filter, this second filter requires input from a sensor independent from the TAM in order to make misalignments observable. The angle between the measured magnetic field vector and, say, the measured sun vector, is differenced from its expected counterpart. This value is used as innovation for the misalignment-estimating Kalman filter.

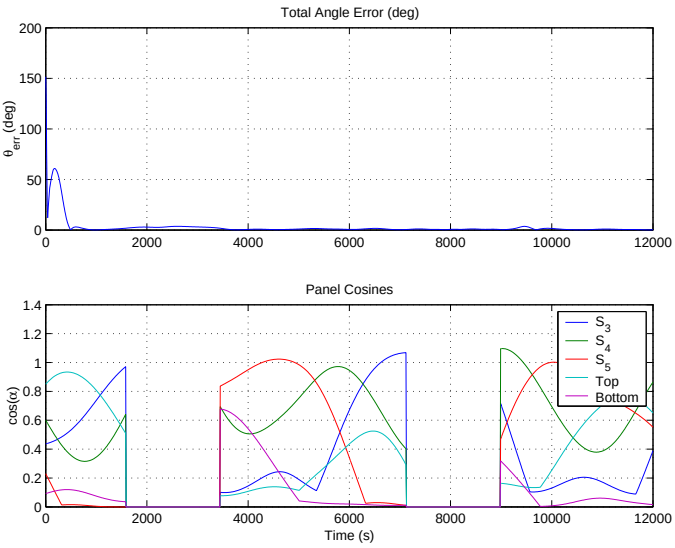

Fig. 12. The initial conditions of Fig. 8 were used now with solar panel data added to the filter. The benefit of the additional data is apparent in the swift convergence. The lower figure indicates availability and intensity of light incident on the solar panels.

This second filter was implemented using solar panel data as the independent measurement. A TAM misalignment of 2° in pitch, 2° in roll, and 3° in yaw was added to the simulator. Estimation of the misalignment was slow due to the inaccuracy of solar panel measurements and strong time correlation of albedo-induced errors, but the misalignment was eventually reduced to tolerable levels. This is reported in Fig. 13. Of course, more accurate sensors may also used as independent measurements with swifter and more accurate results.

The possibility of such thorough TAM calibration means that the TAM used for modestly accurate magnetometer-based attitude estimation need not be mounted on a 6 meter precision machined boom, but may be included within the SC, and may be mounted imprecisely, as on a printed circuit board.

VII. Conclusion

The ION-F satellite cluster will rely on an attitude determination backbone that uses the magnetometer as principal attitude sensor. The backbone stands as an independent, reliable, and inexpensive attitude estimation platform to which other sensors may be added to increase accuracy and speed convergence. Software testing will continue during the summer of 2002 with an emphasis on supervisory attitude software for graceful contingency handling

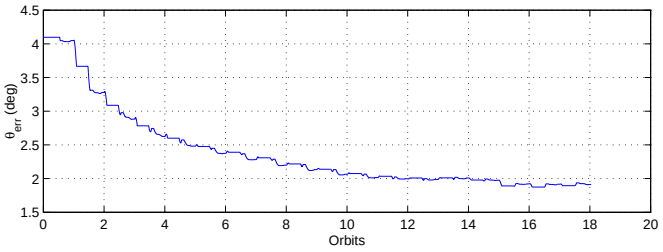

Fig. 13. Estimation of magnetometer misalignments using solar panel data. Error reduction is slow but eventual.

and attitude mode switching. As of May, 2002, the estimation algorithms have been converted to C++ and are being tested on the ION-F CPU, which is handling the demanding computations splendidly. The attitude determination backbone presented in this work, along with the ION-F spacecraft as integrated units, will serve to clear the brush for future student satellites of even greater complexity and possibility.

Acknowledgments

The author would like to thank Dr. Rees Fullmer and Dr. Charles Swenson of Utah State University and the Rocky Mountain Nasa Space Grant Consortium for financial and material support of this work, along with Dr. Thomas Bak of Aalborg University for his generous advice and access to Øersted data and Murty Challa of Computer Sciences Corp. for his comments and encouragement.

VIII. Appendix

A. Reference Frames

For the purposes of filter devopment, a minimal set of reference frames is introduced. The orientation of SC body coordinate system (CS) is determined by the SC inertia tensor with its origin at the SC center of mass. When represented in the SC body CS, the inertia tensor is diagonal. Another reference frame, the SC body-geometric CS, is aligned with geometric features of the SC. Due to symmetry, the body CS for ION-F SC will be close to the body-geometric CS.

A reference frame in which the magnetic field vector and the sun vector are known is generically referred to as the *reference CS*, or *reference frame*. This may be an inertial or non-inertial CS, as long as directional and rate vectors are modified accordingly. In this work, the Earth-centered-inertial (ECI) CS is chosen a the reference CS. Calculation of the Earth magnetic field is performed in the Earth-centered-fixed (ECF) CS.

B. Attitude Parameterization

The SC attitude is parameterized by the 4x1 quaternion, $\bar{q}$, and the 3x3 direction-cosine matrix, A. The quaternion is composed of a vector and scalar part.

$$\bar{q} = \begin{bmatrix} q \\ q_4 \end{bmatrix} \tag{8}$$

with

$$q = \hat{e}\sin(\theta/2), \quad q_4 = \cos(\theta/2) \tag{9}$$

Here, $\hat{e}$ is a unit vector corresponding to the axis of rotation and θ is the angle of rotation. The elements of the quaternion possess only three degrees of freedom and satisfy the constraint $\bar{q}^T\bar{q} = 1$. The direction-cosine matrix A is related to the quaternion by

$$A(\bar{q}) = \begin{bmatrix} q_1^2-q_2^2-q_3^2+q_4^2 & 2(q_1q_2+q_3q_4) & 2(q_1q_3-q_2q_4) \\ 2(q_1q_2-q_3q_4) & -q_1^2+q_2^2-q_3^2+q_4^2 & 2(q_2q_3+q_1q_4) \\ 2(q_1q_3+q_2q_4) & 2(q_2q_3-q_1q_4) & -q_1^2-q_2^2+q_3^2+q_4^2 \end{bmatrix} \tag{10}$$

This may also be written

$$A(\bar{q}) = (q_4^2 - ||q||^2)I_{3\times 3} + 2qq^T - 2q_4[q\times] \tag{11}$$

The skew-symmetric matrix $[q\times]$ defined as

$$[q\times] = \begin{bmatrix} 0 & -q_3 & q_2 \\ q_3 & 0 & -q_1 \\ -q_2 & q_1 & 0 \end{bmatrix} \tag{12}$$

is the *cross-product equivalent matrix* and will be used often in the derivations that follow.

The convention here used for A is that A casts a vector written in the reference frame into body frame coordinates, i.e.,

$$b = Ar \tag{13}$$

The product of two quaternions follows the same ordering convention as the matrix product. Thus,

$$A(\bar{q}')A(\bar{q}) = \bar{q}' \otimes \bar{q} \tag{14}$$

The quaternion product operation $\otimes$ is most easily expressed as a matrix product

$$\bar{q}' \otimes \bar{q} = [\bar{q}']\bar{q} \tag{15}$$

where

$$[\bar{q}'] = \begin{bmatrix} q_4' & q_3' & -q_2' & q_1' \\ -q_3' & q_4' & q_1' & q_2' \\ q_2' & -q_1' & q_4' & q_3' \\ -q_1' & -q_2' & -q_3' & q_4' \end{bmatrix} \tag{16}$$

or alternatively, as

$$\bar{q}' \otimes \bar{q} = \{\bar{q}\}\bar{q}' \tag{17}$$

where

$$\{\bar{q}\} = [\Xi(\bar{q})|\bar{q}] \tag{18}$$

with the 4×3 matrix $\Xi(\bar{q})$ defined in the next section.

C. Attitude Dynamics

Euler's equation expresses the fundamental relationship between external moments applied to the SC and the time rate of change of the angular momentum vector, L.

$$n_{ext} = \left(\frac{dL}{dt}\right)_I = \left(\frac{dL}{dt}\right)_B + [\omega\times]L \tag{19}$$

Here the subscripts I and B denote that the derivative is taken with respect to the inertial or body frame. The angular momentum vector L is the product of the 3×3 inertia matrix I and the angular velocity vector: $L = I\omega$. There always exists a reference frame in which I is a diagonal matrix. This is called a *principal reference frame*. The SC body CS is a principal reference frame, and hence I will always be diagonal with principal moments of inertia I_{xx}, I_{yy}, and I_{zz} when expressed in the body CS.

Euler's equation may be rewritten to isolate the time derivative of ω:

$$\dot{\omega} = I^{-1}(-[\omega\times]I\omega + n_c + n_d) \tag{20}$$

Here, n_{ext} has been broken down into control and disturbance components

$$n_{ext} = n_c + n_d \tag{21}$$

The time evolution of the quaternion is as

$$\dot{\bar{q}} = \frac{1}{2}\Omega(\omega)\bar{q} \tag{22}$$

with

$$\Omega(\omega) = \begin{bmatrix} 0 & \omega_3 & -\omega_2 & \omega_1 \\ -\omega_3 & 0 & \omega_1 & \omega_2 \\ \omega_2 & -\omega_1 & 0 & \omega_3 \\ -\omega_1 & -\omega_2 & -\omega_3 & 0 \end{bmatrix} \tag{23}$$

For small sampling intervals h, the quaternion may be propagated according to

$$\bar{q}_k = \left[I_{4\times 4}\cos\left(\frac{\lambda h}{2}\right) + \Omega(\omega)\frac{\sin\left(\frac{\lambda h}{2}\right)}{\lambda} \right]\bar{q}_{k-1} \tag{24}$$

where $\lambda = ||\omega||$. This equation is useful for propagation. Also useful is the 4×3 matrix $\Xi(\bar{q})$ defined by

$$\Omega(b)\bar{q} = \Xi(\bar{q})b, \quad \Xi(\bar{q}) = \begin{bmatrix} q_4 & -q_3 & q_2 \\ q_3 & q_4 & -q_1 \\ -q_2 & q_1 & q_4 \\ -q_1 & -q_2 & -q_3 \end{bmatrix} \tag{25}$$

D. Kalman Filtering

A review of extended Kalman filtering concepts is included here to provide notational consistency.

The state vector x evolves according to the state equation

$$\dot{x}(t) = f(x(t), u(t), t) + w(t) \tag{26}$$

where $f(x(t), u(t), t)$ is a nonlinear function of the state and control vectors. The process noise $w(t)$ is zero-mean white noise described by the process noise matrix Q.

$$E[w(t)w^T(t')] = Q(t)\delta(t - t') \tag{27}$$

Measurements are assumed to be a nonlinear function of the state, taken at discrete time intervals, and corrupted by measurement noise v.

$$z_k = h(x_k) + v_k \tag{28}$$

The discrete noise sequence v_k is uncorrelated and zero-mean with covariance

$$E[v_k v_s^T] = R_k\delta_{k,s} \tag{29}$$

In the extended Kalman filter (EKF), nonlinear functions are linearized for use in propagating the matrix Ricatti equations and computing the Kalman gain. If the state error vector is defined as the difference between the true state and the state estimate

$$\Delta x = x - \hat{x} \tag{30}$$

then a first-order linear approximation is written

$$\Delta\dot{x}(t) = F(t)\Delta x(t) + G(t)\Delta u(t) + w(t) \tag{31}$$

To arrive at F and G, the function $f(x, u, t)$ is linearized about the state estimate. The Kalman filter produces both pre-measurement and post-measurement state estimates, and the philosophy of the extended Kalman filter is to use the best state estimate available at the time linearization is required. For now, this will be denoted generically as $\hat{x}$. Hence,

$$F(t) = \frac{\partial f(x,u,t)}{\partial x}|_{x=\hat{x}}, \quad G(t) = \frac{\partial f(x,u,t)}{\partial u}|_{x=\hat{x}} \tag{32}$$

The linearized measurement equation is given by

$$\Delta z_k = H_k\Delta x_k + v_k \tag{33}$$

where Δz_k, the *innovation*, contains the new information provided by the latest measurement, and is defined by

$$\Delta z_k = z_k - \hat{z}_k = z_k - h(\hat{x}_k) \tag{34}$$

The measurement sensitivity matrix H_k is found by linearizing $h(x_k)$ about the current best state estimate

$$H_k = \frac{\partial h(x)}{\partial x}|_{x=\hat{x}_k} \tag{35}$$

The continuous Kalman filtering equations are now discretized in order to propagate the Ricatti equations at each sampling step. $F(t)$ is assumed constant over the sampling interval, and discretized according to

$$\Phi(t) = e^{Ft}, \quad \Phi_k \equiv \Phi(T_s) \tag{36}$$

The matrix Φ_k is called the *state transition matrix*. Discrete versions of $G(t)$ and $Q(t)$ may be found by

$$G_k = \int_0^{T_s}\Phi(t)G\,dt, \quad Q_k = \int_0^{T_s}\Phi(t)Q\Phi^T(t)\,dt \tag{37}$$

Here again it is assumed that G and Q are approximately constant over the sampling interval T_s. Furthermore, u is assumed constant over the sampling interval.

The discrete, linear state space model may now be summarized as follows

$$\Delta x_{k+1} = \Phi_k\Delta x_k + G_k u_k + w_k \tag{38}$$

$$\Delta z_k = H_k\Delta x_k + v_k \tag{39}$$

The Kalman filter is applied to this model.

In practice, the state transition matrix is not used in the propagation step (time update) of the Kalman filter. Rather, the nonlinear dynamics equations are numerically integrated with an integration step much smaller than T_s. The state transition matrix is used for the propagation of the discrete Ricatti equations. Because the accuracy of these computations is not needed at the same level as the state vector propagation, the transition matrix is usually approximated using only the first few terms of the Taylor series expansion of e^{FT_s}, i.e.,

$$\Phi_k \approx I + FT_s \tag{40}$$

The extended Kalman filtering equations are summarized as follows:

Initialization

- Begin with an initial estimate of the state, $\hat{x}_{0|0}$
- Reflect the uncertainty in the initial estimate in the initial error covariance matrix, $P_{0|0}$

Prediction (Time Update)

- Numerically integrate the nonlinear dynamics equations using $\hat{x}_{k|k}$ as the initial condition to obtain a predicted estimate of the state. Call this estimate $\hat{x}_{k+1|k}$. It represents the estimate of the state at step $k+1$ given the previous k measurements.
- Compute the state transition matrix

$$\Phi_k \approx I + FT_s \tag{41}$$

F is a linearization of the system dynamics equations about $\hat{x}_{k|k}$.

- Compute the process noise covariance matrix

$$Q_k = \int_0^{T_s} \Phi(t) Q \Phi^T(t)\, dt \tag{42}$$

- Update the error covariance matrix

$$P_{k+1|k} = \Phi_k P_{k|k} \Phi_k^T + Q_k \tag{43}$$

Filtering (Measurement Update)

- Update the measurement sensitivity matrix by linearizing about the current best state estimate

$$H_{k+1|k} = \frac{\partial h(x)}{\partial x}|_{x=\hat{x}_{k+1|k}} \tag{44}$$

- Compute the Kalman gain

$$K_{k+1} = P_{k+1|k} H_{k+1|k}^T (H_{k+1|k} P_{k+1|k} H_{k+1|k}^T + R_{k+1})^{-1} \tag{45}$$

- Update the state error estimate

$$\Delta\hat{x}_{k+1|k+1} = \Delta\hat{x}_{k+1|k} + K_{k+1}(\Delta z_{k+1} - H_{k+1|k}\Delta x_{k+1|k}) \tag{46}$$

This may be simplified by noting that by definition

$$\Delta\hat{x}_{k+1|k} = \hat{x}_{k+1|k} - \hat{x}_{k+1|k} = 0 \tag{47}$$

and rewriting

$$\Delta\hat{x}_{k+1|k+1} = K_{k+1}(\Delta z_{k+1}) = K_{k+1}(z_{k+1} - h(\hat{x}_{k+1|k})) \tag{48}$$

- Add the state error estimate to the predicted state estimate to obtain the filtered (post-measurement) state estimate

$$\hat{x}_{k+1|k+1} = \hat{x}_{k+1|k} + \Delta\hat{x}_{k+1|k+1} \tag{49}$$

- Update the measurement sensitivity matrix using the filtered state estimate. Note that this second update of H is not a part of the traditional EKF. It is included to bring about a more rapid decrease in the value of the error covariance matrix P. Without this modification, large initial state errors frequently cause P to grow sharply at first, making convergence difficult.

$$H_{k+1|k+1} = \frac{\partial h(x)}{\partial x}|_{x=\hat{x}_{k+1|k+1}} \tag{50}$$

- Update the error covariance matrix

$$\begin{aligned} P_{k+1|k+1} &= (I - K_{k+1}H_{k+1|k+1})P_{k+1|k}(I - K_{k+1}H_{k+1|k+1})^T \\ &+ K_{k+1}R_{k+1}K_{k+1}^T \end{aligned} \tag{51}$$

E. An EKF for Spacecraft Attitude Determination Based on Magnetometer and Solar Panel Measurements

The dependence of the four quaternion elements given by $\bar{q}^T\bar{q} = 1$ gives rise to an error covariance matrix P that is singular. This follows from the fact that since $\hat{\bar{q}}$ and $\bar{q}$ are each of euclidean length 1, their difference, $\Delta\bar{q}$ must be orthogonal to both $\hat{\bar{q}}$ and $\bar{q}$ as $||\Delta\bar{q}|| \to 0$. Hence, $\Delta\bar{q}^T\hat{\bar{q}} \approx 0$, and

$$\begin{bmatrix} \hat{\bar{q}} \\ 0_{6\times 1} \end{bmatrix} \tag{52}$$

is a null vector of P. Maintaining the singularity of P is made difficult because of round-off error accumulation. There are several ways to deal with this issue. One may simply ignore the singularity of P, and treat each of the quaternion elements as independent in the filtering process. Normalization of the quaternion external to the filter becomes necessary, and this represents an outside interference which must be taken into account. No effort is made to maintain the singularity of P. This method works reasonably well in practice, although propagation of the outside interference constitutes an additional computational expense [13].

Another method described in Lefferts et al.[14] is adapted for use in the sequel.

Typical attitude determination is concerned with estimating the SC attitude (as parameterized by the quaternion) and angular rate. In the absence of rate gyros, both the quaternion and angular rate vector are included in the state to be estimated. For added robustness and accuracy in the face of slowly varying disturbance torques, an estimate of the disturbance torque vector, n_d, is also included in the state estimate [5]. The full 10-dimensional state is then

$$x = \begin{bmatrix} \bar{q} \\ \omega \\ n_d \end{bmatrix} \tag{53}$$

In order to represent the state without the quaternion redundancy, a 9×1 body-referenced state vector is defined as

$$\tilde{x} = \begin{bmatrix} \delta q \\ \omega \\ n_d \end{bmatrix} \tag{54}$$

The quantity δq is called the vector component of the error quaternion. The error quaternion is defined implicitly by

$$\bar{q} = \delta\bar{q} \otimes \hat{\bar{q}} \tag{55}$$

Because the error quaternion corresponds almost certainly to a small rotation, the fourth component will be close to unity. But during initial convergence, this approximation is often violated. This is accounted for in section III-B found in the main body of this work. In general, it is assumed that θ is sufficiently small. Hence, all attitude information of interest is contained in the vector part of the error quaternion, δq. Using (18), the quaternion composition is rewritten as a matrix product

$$\bar{q} = \delta\bar{q} \otimes \hat{\bar{q}} = [\Xi(\hat{\bar{q}})|\hat{\bar{q}}]\delta\bar{q} \tag{56}$$

The normalization constraint on the quaternion gives rise to the following three properties involving $\Xi(\bar{q})$:

$$\Xi^T(\bar{q})\bar{q} = 0 \tag{57}$$

$$\bar{q}^T\Xi(\bar{q}) = 0 \tag{58}$$

$$\Xi^T(\bar{q})\Xi(\bar{q}) = I_{3\times 3} \tag{59}$$

Using these properties, it follows easily that

$$\delta q = \Xi^T(\hat{\bar{q}})\bar{q} \tag{60}$$

$$\delta q_4 = \hat{\bar{q}}^T\bar{q} \tag{61}$$

The body-referenced state vector may now be related to the standard state vector

$$\begin{bmatrix} \delta q \\ \omega \\ n_d \end{bmatrix} = \begin{bmatrix} \Xi^T(\hat{\bar{q}}) & 0_{3\times 6} \\ 0_{6\times 4} & I_{6\times 6} \end{bmatrix} \begin{bmatrix} \bar{q} \\ \omega \\ n_d \end{bmatrix} \tag{62}$$

or

$$\tilde{x} = S^T(\hat{\bar{q}})x \tag{63}$$

By noting that

$$\hat{\tilde{x}} = S^T(\hat{\bar{q}})\hat{x} = \begin{bmatrix} 0 \\ \omega \\ n_d \end{bmatrix} \tag{64}$$

the vector $\Delta\tilde{x} \equiv \tilde{x} - \hat{\tilde{x}}$ becomes

$$\Delta\tilde{x} = \begin{bmatrix} \delta q \\ \Delta\omega \\ \Delta n_d \end{bmatrix} \tag{65}$$

This 9-dimensional body-referenced state error vector is the state vector for the linearized dynamics and measurement equations

$$\Delta\dot{\tilde{x}}(t) = F(t)\Delta\tilde{x}(t) + G(t)\Delta u(t) + w(t) \tag{66}$$

$$\Delta z_k = H_k\Delta\tilde{x} + v_k \tag{67}$$

Attention now turns to finding explicit forms for $F(t)$ and H_k. It isn't necessary to find $G(t)$ since numerical integration is used to propagate the state, and only the discretized version of $F(t)$ is necessary for propagating the matrix Ricatti equations.

$F(t)$ is formed by linearizing the state dynamics equations about a filtered estimate of the state, $\hat{\tilde{x}}_{k|k}$. The nonlinear dynamics equations for propagating $\tilde{x}$ are based on those used for the propagation of x, which are

$$\dot{\bar{q}} = \frac{1}{2}\Omega(\omega)\bar{q} \tag{68}$$

$$\dot{\omega} = I^{-1}(-[\omega\times]I\omega + n_d + n_c) \tag{69}$$

$$\dot{n}_d = 0 \tag{70}$$

Focusing first on the quaternion update, an expression must be found for the linear time evolution of δq. In other words, $F_1(t)$ in the equation

$$\delta\dot{q}(t) = F_1(t)\Delta\tilde{x}(t) + G_1(t)\Delta u(t) + w_1(t) \tag{71}$$

is sought. Equations useful for deriving F_1 are repeated here for convenience

$$\bar{q} = \delta\bar{q} \otimes \hat{\bar{q}} \tag{72}$$

$$\dot{\bar{q}} = \frac{1}{2}\Omega(\omega)\bar{q} \tag{73}$$

$$\dot{\hat{\bar{q}}} = \frac{1}{2}\Omega(\hat{\omega})\hat{\bar{q}} \tag{74}$$

Also useful are the following properties of quaternion composition:

- Association

$$(\bar{a} \otimes \bar{b}) \otimes \bar{c} = \bar{a} \otimes (\bar{b} \otimes \bar{c}) \tag{75}$$

- Commutative relation

$$\bar{a} \otimes \bar{b} = \bar{b} \otimes \bar{a} + 2\begin{bmatrix} b \times a \\ 0 \end{bmatrix} \tag{76}$$

- Product rule for quaternion composition

$$\frac{d}{dt}\left(\bar{a} \otimes \bar{b}\right) = \left(\frac{d}{dt}\bar{a}\right) \otimes \bar{b} + \bar{a} \otimes \left(\frac{d}{dt}\bar{b}\right) \tag{77}$$

Applying the product rule to (72) yields

$$\dot{\bar{q}} = \delta\dot{\bar{q}} \otimes \hat{\bar{q}} + \delta\bar{q} \otimes \dot{\hat{\bar{q}}} \tag{78}$$

into which the definitions for the derivatives are substituted

$$\frac{1}{2}\Omega(\omega)\bar{q} = \delta\dot{\bar{q}} \otimes \hat{\bar{q}} + \frac{1}{2}\delta\bar{q} \otimes \Omega(\hat{\omega})\hat{\bar{q}} \tag{79}$$

Rearranging, and using the quaternion inverse $\bar{q}^{-1}$ defined by

$$\bar{q} \otimes \bar{q}^{-1} = [0, 0, 0, 1]^T \tag{80}$$

yields

$$\delta\dot{\bar{q}} = \frac{1}{2}\Omega(\omega)\bar{q} \otimes \hat{\bar{q}}^{-1} - \frac{1}{2}\delta\bar{q} \otimes \Omega(\hat{\omega})[0,0,0,1]^T \tag{81}$$

But, by definition,

$$\delta\bar{q} = \bar{q} \otimes \hat{\bar{q}}^{-1} \tag{82}$$

yielding

$$\delta\dot{\bar{q}} = \frac{1}{2}\Omega(\omega)\delta\bar{q} - \frac{1}{2}\delta\bar{q} \otimes \Omega(\hat{\omega})[0,0,0,1]^T \tag{83}$$

Let

$$\bar{\omega} = \begin{bmatrix} \omega \\ 0 \end{bmatrix} \tag{84}$$

then further simplification yields

$$\delta\dot{\bar{q}} = \frac{1}{2}\Omega(\omega)\delta\bar{q} - \frac{1}{2}\delta\bar{q} \otimes \hat{\bar{\omega}} \tag{85}$$

Noting that $\Omega(\bar{q})$ is linear in its elements,

$$\Omega(\omega) = \Omega(\hat{\omega} + \Delta\omega) = \Omega(\hat{\omega}) + \Omega(\Delta\omega) \tag{86}$$

and invoking the commutative relation yields, after some cancellation

$$\delta\dot{\bar{q}} = \begin{bmatrix} -[\hat{\omega}\times]\delta q \\ 0 \end{bmatrix} + \frac{1}{2}\Omega(\Delta\omega)\delta\bar{q} \tag{87}$$

The following is observed about the second term on the right hand side:

$$\Omega(\Delta\omega)\delta\bar{q} = \begin{bmatrix} \Delta\omega \\ 0 \end{bmatrix} \delta q_4 + HOT \tag{88}$$

where $\delta q_4 \approx 1$ and HOT is made up of negligible second-order terms. With this approximation,

$$\delta\dot{\bar{q}} = \begin{bmatrix} -[\hat{\omega}\times]\delta q \\ 0 \end{bmatrix} + \frac{1}{2}\begin{bmatrix} \Delta\omega \\ 0 \end{bmatrix} \tag{89}$$

from which the desired expression for F_1 is extracted

$$F_1 = \left[-[\hat{\omega}\times] \left| \frac{1}{2} I_{3\times 3} \right| 0_{3\times 3} \right] \tag{90}$$

The second component of the dynamics matrix, F_2 defined by

$$\Delta\dot{w}(t) = F_2(t)\Delta\tilde{x}(t) + G_2(t)\Delta u(t) + w_2(t) \tag{91}$$

is found by straightforward linearization of

$$f_2(\tilde{x}) = I^{-1}(-[\omega\times]I\omega + n_d + n_c) \tag{92}$$

so that

$$F_2 = \frac{\partial f_2(\tilde{x})}{\partial \tilde{x}}|_{\tilde{x}=\hat{\tilde{x}}_{k|k}} = \left[0_{3\times 3} \left|\Theta(\hat{\omega})\right| I^{-1}\right] \tag{93}$$

where

$$\Theta(\hat{\omega}) = \frac{df_2(\tilde{x})}{d\omega}|_{\tilde{x}=\hat{\tilde{x}}_{k|k}} \tag{94}$$

may be written explicitly for a diagonal inertia tensor I as

$$\Theta(\hat{\omega}) = \begin{bmatrix} 0 & \frac{\hat{\omega}_3\,(Iyy-Izz)}{Ixx} & \frac{\hat{\omega}_2\,(Iyy-Izz)}{Ixx} \\ \frac{\hat{\omega}_3\,(Izz-Ixx)}{Iyy} & 0 & \frac{\hat{\omega}_1\,(Izz-Ixx)}{Iyy} \\ \frac{\hat{\omega}_2\,(Ixx-Iyy)}{Izz} & \frac{\hat{\omega}_1\,(Ixx-Iyy)}{Izz} & 0 \end{bmatrix} \tag{95}$$

Finally, F_3, defined by

$$\Delta\dot{n}_d(t) = F_3(t)\Delta\tilde{x}(t) + G_3(t)\Delta u(t) + w_3(t) \tag{96}$$

is simply

$$F_3 = [0_{3\times 9}] \tag{97}$$

by (70). Combining F_1, F_2 and F_3, yields the linearized dynamics matrix

$$F = \begin{bmatrix} F_1 \\ F_2 \\ F_3 \end{bmatrix} = \begin{bmatrix} -[\hat{\omega}\times] & \frac{1}{2}I_{3\times 3} & 0_{3\times 3} \\ 0_{3\times 3} & \Theta(\hat{\omega}) & I^{-1} \\ 0_{3\times 3} & 0_{3\times 3} & 0_{3\times 3} \end{bmatrix} \tag{98}$$

Attention now turns to finding a linearization for the measurement equation. That is, H_k is sought such that to first order

$$\Delta z_k = H_k\Delta\tilde{x} + v_k \tag{99}$$

As mentioned previously, Δz_k is referred to as the *innovation* and is defined for the classical EKF as

$$\Delta z_k = z_k - h(\hat{\tilde{x}}_{k|k-1}) \tag{100}$$

This definition differs from the innovation used in [5], which is based on a cross-product. The present definition is preferred where mispointings may exceed 90° and ambiguity would arise using the cross-product. The physical significance of the cross-product innovation as reported in [5] is useful for interpretation, but provides no advantage over the classical innovation for overall filter accuracy. For the present filter, the measurement z_k contains the normalized magnetic field reading from the TAM, and may be augmented by scalar readings from the solar panels. Scalar solar panel readings are based on the relation

$$\frac{i(\alpha)}{i(0)} = \cos(\alpha) = p^T s^B \tag{101}$$

which equates a normalized panel current reading to the inner product of the unit vector normal to the panel, p, and the normalized sun vector in body coordinates, s^B, where α is the sunlight incidence angle. The measurement z_k then becomes

$$z_k = h(\tilde{x}_k) + v_k = \begin{bmatrix} A(\bar{q})b_k \\ p_1^T A(\bar{q})s_k \\ p_2^T A(\bar{q})s_k \\ \vdots \\ p_N^T A(\bar{q})s_k \end{bmatrix} + v_k \tag{102}$$

where b_k and s_k are the magnetic field and sun vectors in the reference CS, and N is the number of sunlit solar

panels. To find H_k, $h(\tilde{x}_k)$ is linearized about the current best state estimate, $\hat{\tilde{x}}_k$

$$H_k = \frac{\partial h(\tilde{x})}{\partial \tilde{x}}|_{\tilde{x}=\hat{\tilde{x}}_k} \tag{103}$$

To this end, $A(\bar{q})$ is rewritten as the product of factors

$$A(\bar{q}) = A(\delta\bar{q})A(\hat{\bar{q}}) \tag{104}$$

The estimated magnetic field and sun vectors in body coordinates

$$\hat{b}_k^B \equiv A(\hat{\bar{q}})b_k, \quad \hat{s}_k^B \equiv A(\hat{\bar{q}})s_k \tag{105}$$

do not depend on any of the elements of the state $\tilde{x}$, and may be regarded as multiplicative constants. The rotation matrix $A(\delta\bar{q})$ does depend on state elements, and is linearized by neglecting second-order terms

$$A(\delta\bar{q}) \approx I_{3\times 3} - 2[\delta q\times] \tag{106}$$

The derivative of

$$h(\tilde{x}) = \begin{bmatrix} (I_{3\times 3} - 2[\delta q\times])\hat{b}_k^B \\ (I_{3\times 3} - 2[\delta q\times])\hat{s}_k^B \\ \vdots \\ (I_{3\times 3} - 2[\delta q\times])\hat{s}_k^B \end{bmatrix} \tag{107}$$

is now effected by simple extraction of the linear terms

$$H_k = \frac{\partial h(\tilde{x})}{\partial \tilde{x}}|_{\tilde{x}=\hat{\tilde{x}}_k} = \begin{bmatrix} 2[\hat{b}_k^B\times] & 0_{3\times 6} \\ 2p_1^T[\hat{s}_k^B\times] & 0_{1\times 6} \\ \vdots & \vdots \\ 2p_N^T[\hat{s}_k^B\times] & 0_{1\times 6} \end{bmatrix} \tag{108}$$

References

[1] QRS11 Micromachined Angular Rate Sensor data sheet. Systron Donner. Available at: http://www.systron.com

[2] Model 533 Miniature 3-Axis Fluxgate Magnetometer data sheet. Applied Physics. Available at: http://www.appliedphysics.com

[3] Psiaki, M.L., "Attitude Sensing Using a Global-Positioning-System on a Turntable", AIAA Paper AIAA-2000-3947, 2000.

[4] Shucker, B., "A Ground-Based Prototype of a CMOS Navigational Star Camera for Small Satellite Applications," AIAA/Utah State University Small Satellite Conference, SSC-01-VII-3, August 2001.

[5] Psiaki, M.L., Martel, F., and Pal, P.K., "Three-Axis Attitude Determination via Kalman Filtering of Magnetometer Data", *Journal of Guidance, Control, and Dynamics*, Vol. 13, No.3,1989, pp. 506 - 514.

[6] *Astronomical Almanac for the Year 2001* U.S. G.P.O. pp. C24

[7] Cunningham, F.G., NASA Technical Note D-710, August, 1961

[8] *NASA TM 4527*,pp. 9-10

[9] "Qualification Test Report for Commercial Cascade TEC3i Solar Cell/CIC," TECHSTAR. Inc. (now Emcore) August, 2001.

[10] Steyn, W.H., Hashida, Y., and Lappas, V., "An Attitude Control System and Commissioning Results of the SNAP-1 Nanosatellite," AIAA/Utah State University Small Satellite Conference, SSC00-VIII-8, August, 2000.

[11] Challa, M., Natanson, G., Deutschmann, J., and Galal, K., "A PC-Based Magnetometer-Only Attitude and Rate Determination System for Gyroless Spacecraft," *Proceedings of the NASA/GSFC Flight Mechanics/Estimation Theory Symposium*, May 16-18, 1995, paper No. 7.

[12] Landiech, P., "Extensive Use of Magnetometers and Magnetotorquers for Small Satellites Attitude Estimation and Control", AIAA Paper AAS 95-012, 1995.

[13] Bar-Itzhack, I.Y., Deutchmann, J., and Markley, F.L., "Quaternion Normalization in Additive EKF for Spacecraft Attitude Determination", AIAA Paper AIAA-91-2706-CP, 1991.

[14] Lefferts, E.J., Markley, F.L., and Shuster, M.D., "Kalman Filtering for Spacecraft Attitude Estimation", *Journal of Guidance, Control, and Dynamics*, Vol. 5, No.5, Sept.-Oct. 1982, pp. 417 - 429.

[15] Wertz, J.R., (ed.), *Spacecraft Attitude Determination and Control*, Kluwer, 1991.

[16] Zarchan, P. and Musoff, H., *Fundamentals of Kalman Filtering*, AIAA Progress in Astronautics and Aeronautics, Vol. 190, 2000.

[17] Moon, T.K. and Stirling, W.C., *Mathematical Methods and Algorithms for Signal Processing*, Prentice Hall, 2000.

[18] Bar-Itzhack, I.Y., and Oshman, Y., "Attitude Determination from Vector Observations: Quaternion Estimation", IEEE Trans. on Aerospace and Electronic Systems Vol. AES-21, No. 1, Jan. 1985

[19] Woodham, K., Blackman, K., and Sanneman, P., "Solar and Magnetic Attitude Determination for Small Spacecraft", AIAA Paper A97-32198, 1997.